PUBLICATIONS OF THE ASTRONOMICAL SOCIETY OF THE PACIFIC, 111:691–701, 1999 June
© 1999. The Astronomical Society of the Pacific. All rights reserved. Printed in U.S.A.

The Detection and Photometric Redshift Determination of Distant Galaxies Using *SIRTF*'s Infrared Array Camera

CHRIS SIMPSON[1] AND PETER EISENHARDT

Jet Propulsion Laboratory, California Institute of Technology, Mail Stop 169-327, 4800 Oak Grove Drive, Pasadena, CA 91109; chris@naoj.org

Received 1998 April 9; accepted 1999 March 1

ABSTRACT. We investigate the ability of the *Space Infrared Telescope Facility*'s Infrared Array Camera to detect distant ($z \sim 3$) galaxies and measure their photometric redshifts. Our analysis shows that changing the original long-wavelength filter specifications provides significant improvements in performance in this and other areas.

1. INTRODUCTION

On 1998 March 25, NASA Administrator Daniel Goldin approved the initiation of final design and construction for the *Space Infrared Telescope Facility* (*SIRTF*; Fanson et al. 1998). With launch planned for 2001 December, *SIRTF* will complete NASA's family of Great Observatories. *SIRTF* will provide a large increase in sensitivity over previous missions across its 3–200 μm operating range, and over 75% of the observing time during its 2.5 year minimum lifetime will be awarded to general investigators. A call for Legacy Proposals (large projects of both immediate scientific interest and lasting archival value, and with no proprietary data period) is planned for 2000 July.

One of the defining scientific programs for *SIRTF* is the study of galaxies to $z > 3$ by means of deep surveys at 3–10 μm. This limit was selected because it is apparently beyond the peak in the space density of luminous quasars (Schmidt, Schneider, & Gunn 1995). Not only will *SIRTF*'s excellent sensitivity in this wavelength region allow such galaxies to be detected with the Infrared Array Camera (IRAC; Fazio et al. 1998), but the H^- opacity minimum at 1.6 μm (John 1988) is expected to be a major tool in photometric redshift determination at $1 \lesssim z \lesssim 5$ (Wright, Eisenhardt, & Fazio 1994), since it is a ubiquitous feature of stellar atmospheres.

UV-bright examples of such galaxies have already been detected by means of the "UV-dropout" technique (Steidel & Hamilton 1992, 1993; Steidel et al. 1996), and they play an important role in the overall star formation history of the universe (Madau et al. 1996). By detecting galaxies on the strength of their UV emission, however, UV-dropout samples are necessarily biased in favor of those with both active star formation and relatively modest extinction. Such samples will not reveal whether there is an underlying population of galaxies which have already assembled the bulk of their stellar mass. In the absence of ongoing star formation, even massive galaxies will be too faint in the rest-frame ultraviolet to be picked up by optical surveys. The stellar mass already present at an early epoch constrains the star formation rate to that point, a quantity which is still uncertain because of the possibility of significant dust extinction. Steidel et al. (1999) suggest that "the onset of substantial star formation activity in galaxies might occur at $z > 4.5$" and estimate the net extinction correction to the star formation rate derived from UV dropouts to be a factor of about 5. Recent far-infrared detections of the cosmic background (Hauser et al. 1998), and far-infrared and submillimeter detections of field galaxies with *Infrared Space Observatory* and Submillimetre Common-User Bolometer Array (SCUBA; Kawara et al. 1998; Puget et al. 1999; Barger et al. 1998; Hughes et al. 1998), also hint at a heavily dust enshrouded starburst population. Hence an accurate picture of the star formation history of the universe can only be determined by making an accurate census of *all* galaxies, not just star-forming ones with low extinction. Since the luminosity in the rest-frame near-infrared correlates linearly with mass (Gavazzi, Peirini, & Boselli 1996) and is relatively unaffected by dust obscuration, this is clearly the spectral region in which to make such a census.

In this paper we examine changing the specifications of the IRAC filters in order to optimize them for the study of $z \sim 3$ galaxies, including photometric redshift determination. IRAC will have two detector arrays made from indium antimonide (InSb), which is sensitive to $\lambda \lesssim 5$ μm photons, and two made from arsenic-doped silicon (Si:As), which detects longer wavelength light. All four arrays will have a 256 × 256 format, with 1″.2 pixels, and will operate simultaneously. The InSb arrays will have filters centered at 3.63 μm with 20.4% bandwidth and at 4.53 μm with 23.3%

[1] Present address: Subaru Telescope, National Astronomical Observatory of Japan, 650 North A'ohōkū Place, Hilo, HI 96720.

bandwidth. We shall refer to these filters as L and M, respectively, because of their similarity to the filters used in ground-based facilities. The filters for the Si:As arrays have no ground-based analogs, since they cover wavelengths where the atmosphere is opaque, and so we refer to them as A and B, with A being the bluer of the two. The L and A filters share one field and are separated by a dichroic filter, while the M and B filters similarly share a second nearly adjacent field. The original, or "baseline," specifications for A and B are 25% bandwidth filters centered at 6.3 and 8.0 μm. Our analysis will involve comparing the performance of different pairs of filters, and we distinguish between these pairs by the use of subscripts, so for example the baseline filters described above are called A_b and B_b. We also introduce the notation $[\lambda_1 : \lambda_2]$ to describe a filter which extends from λ_1 μm to λ_2 μm. In this notation, the L filter is $[3.26:4.00]$, $M = [4.00:5.06]$, $A_b = [5.51:7.09]$, and $B_b = [7.00:9.00]$.

2. ASSUMPTIONS

The calculations in this paper all assume a total integration time of 10 hr per point (made up of many individual 200 s exposures), which allows a deep image of a large area of sky to be obtained in a sensible integration time. For such exposure times, IRAC requires background-limited operation, and therefore we neglect read noise and dark current. Confusion noise will be discussed in § 5.1 but is otherwise not considered here. As *SIRTF* is required to be diffraction limited at 6.5 μm, we adopt a detection area of 20 pixels, independent of wavelength, and assume that all the source flux is contained within this region.

2.1. Telescope and Instrument Efficiency

The fraction of photons incident upon *SIRTF*'s 85 cm diameter aperture which reach the IRAC detectors is specified in the *SIRTF* Observatory Performance and Interface Control Document (PICD) and the IRAC Instrument Performance Requirements Document[2] and is about 50%, including filter transmission. The InSb quantum efficiency (QE) is assumed to be 80% over the entire wavelength range of the two InSb filters. The QE of the Si:As arrays is based on the average of laboratory measurements made on a number of flight-candidate arrays coated with antireflection coatings of either SiO or ZnS. Because of the high opacity of SiO beyond 8 μm, in the following analysis we assume that the ZnS coating will be used in preference to the SiO coating if the filter bandpass extends beyond 8 μm. The net result of these assumptions is a QE of approximately 60%–65% for the two Si:As filters. We also assume that the various filters considered here are opaque outside their nominal wavelength region.

[2] The *SIRTF* PICD is Jet Propulsion Laboratory document 674–SEIT–100, V2.2. The IPRD is Smithsonian Astrophysical Observatory document IRAC96–202, revision 4.2.

2.2. Background

From the PICD, the minimum *SIRTF* background (which occurs at the ecliptic pole for wavelengths considered here), $b(\lambda)$ is computed as

$$b(\lambda) = 5.5 \times 10^{-14} B_\lambda(5500) + 4.2 \times 10^{-8} B_\lambda(278.5) + 2.5 \times 10^{-4} (\lambda/100\ \mu\text{m})^2 B_\lambda(17.5) + B_\lambda(2.73)\ ,$$

where $B_\lambda(T)$ is the Planck function for a temperature of T K. The first term is due to scattered sunlight from zodiacal dust, the second and third terms to thermal emission from zodiacal and Galactic dust, respectively, and the final term is the cosmic microwave background radiation. This function provides an excellent fit to data from the DIRBE instrument (Hauser 1996).

2.3. Cosmology and Galaxy Models

Our analysis is concerned with the detection of high-redshift galaxies. We construct model spectra of such galaxies using the GISSEL96 spectral synthesis code (Bruzual & Charlot 1993, 1999; see also Charlot, Worthey, & Bressan 1996). This code does not include polycyclic aromatic hydrocarbon (PAH) features at 3.3 μm and beyond, but at $z = 3$ these features are at observed wavelengths beyond the range considered here. We will return to the PAH features when we discuss confusion noise.

We adopt a conservative (in the sense of making $z \sim 3$ galaxies faint) cosmology with $H_0 = 50$ km s^{-1} Mpc^{-1} and $q_0 = 0.1$, corresponding to a present age of the universe of 16.5 Gyr (at $z = 3$ the universe is 2.9 Gyr old). We assume a Salpeter (1955) initial mass function extending from 0.1–125 $M_\odot$, and normalize our galaxies to have $M_K = -24.63$ (L^*; Gardner et al. 1997) at an age of 16.5 Gyr. We use four models to represent the limits of galaxy evolution. Model A is a maximally old model with solar metallicity formed in an instantaneous burst at $z = \infty$ and evolving passively thereafter. Model B is like A but with metallicity only 1/50 solar. As we show in § 3.3, these types of galaxies will not appear in UV-dropout samples. Model C is a young solar-metallicity galaxy formed with a constant star formation rate over the 100 Myr prior to whatever redshift is considered (i.e., a young nonevolving spectrum). Model D is like C, but again with $Z = 0.02\ Z_\odot$. Models C and D are

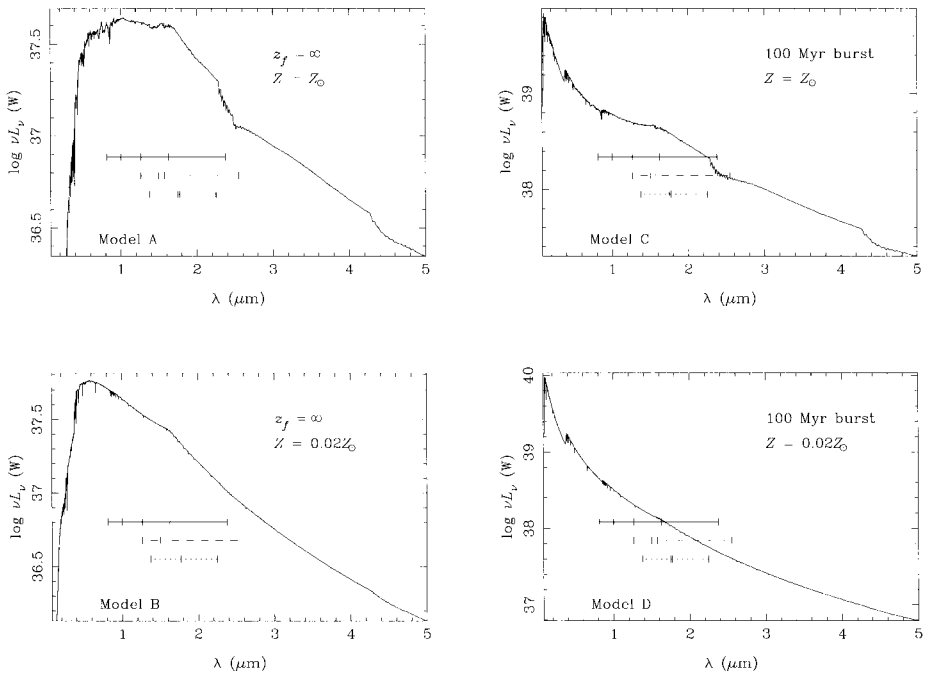

FIG. 1.—The rest-frame spectra at $z = 3$ of the four galaxy models. The solid horizontal bars indicate the preferred filter set, whereas the dashed bars show the optimum Si:As filters and the dotted bars the baseline Si:As filters.

much more luminous than models A and B at $z = 3$ and are representative of the spectra expected for UV-dropout galaxies. The rest-frame ultraviolet-optical-infrared spectra of these four models at $z = 3$ are shown in Figure 1.

The only feature common to all these spectra is a change in slope at 1.6 μm, due to the H^- opacity minimum, although this is barely discernible in Model D. It is in fact the only feature in the two low-metallicity models, which lack the prominent CO bandhead at 2.3 μm and the effects of metal line blanketing at rest-frame optical wavelengths. This therefore makes it a suitable feature for use in photometric redshift determination, a technique whereby an approximate redshift can be inferred from observed colors as one or more spectral features pass through broadband filters (e.g., Hogg et al. 1998).

3. SENSITIVITY

Since *SIRTF*'s observations will be dominated by general observer programs, it is important to consider performance independent of any particular program, in addition to the high-redshift galaxy observations which drive the filter recommendations made here. In fact, as we discuss in § 6, the pair of filters which provide the optimum performance for $A-B$ color selection and photometric redshift determination at $z \sim 3$ are not very suitable for other science programs. For this reason we will throughout the course of this paper be discussing the relative performance of three different Si:As filter pairs, which we designate "baseline," "optimum," and "preferred" and denote by subscripts b, o, and p, respectively. The baseline filters are the two 25% bandwidth filters centered at 6.3 and 8.0 μm, the optimum filters provide the most accurate $A-B$ color selection and photometric redshift determination (see § 4) at $z \sim 3$, and the preferred filters give slightly poorer performance in these areas, but are expected to be much more useful for other scientific programs. The optimum filters are $A_o = [5.06:6.00]$ and $B_o = [6.30:10.20]$, and the preferred filters are $A_p = [5.06:6.50]$ and $B_p = [6.50:9.50]$.

3.1. Power-Law Spectrum Source

Figure 2 is a contour plot of IRAC's background-limited 5 σ sensitivity in 10 hr of integration as a function of filter cut-on and cutoff wavelength for a source which has a flat spectrum in S_ν. Since the contour lines are fairly vertical, it is evident that the cut-on wavelength is more important than the cutoff. It is also clear from this figure that the best sensitivity is achieved for a very blue filter whose short-wavelength cut-on will be constrained by the dichroic response. Within the parameter space plotted, a [4.2:5.7]

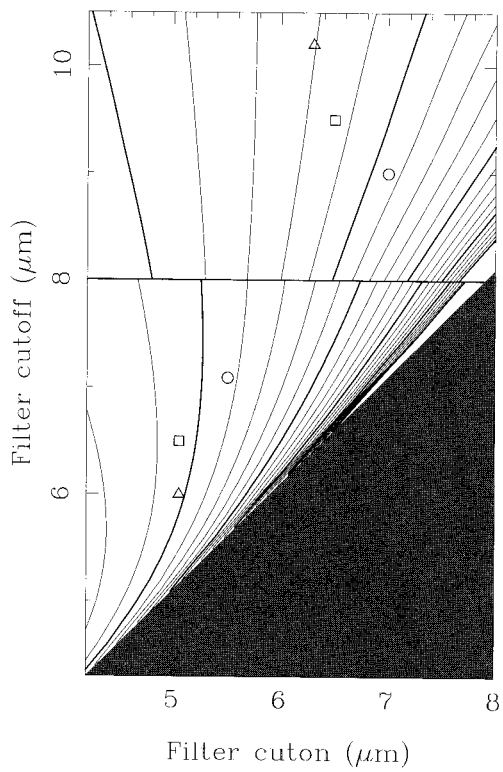

FIG. 2.—Contours of limiting flux in μJy (5 σ, 10 hr) as a function of filter cut-on and cutoff wavelength for a source with a flat spectrum (in S_ν). The contour range is from 0.6 to 5.0 μJy in steps of 0.2 μJy, with heavier lines at 1, 2, 3, 4, 5 μJy. The discontinuity at $\lambda_{cutoff} = 8$ μm is due to the change in coating from SiO to ZnS. Squares mark the preferred filter specifications, triangles the optimum filters, and circles the baseline filters.

filter is most sensitive, with a 5 σ 10 hr limiting flux of 1.1 μJy. However, this filter overlaps the InSb M filter almost entirely, and since InSb has a higher quantum efficiency there is little point in duplicating it. We therefore restrict our analysis to filters with $\lambda_{cuton} > 5.06$ μm (the cutoff of the M filter). The second column in Table 1 lists the sensitivity achieved by various IRAC filters for a flat spectrum source.

TABLE 1

SIGNAL-TO-NOISE RATIOS ACHIEVABLE WITH IRAC IN 10 HOURS

	S/N FOR MODEL				
FILTER	10 μJy	A	B	C	D
Best filter[a]	55.9	26.9	20.0	309	105
λ_{cutoff}[b]	[6.9]	[7.1]	[6.7]	[6.9]	[6.4]
L	232.2	70.9	82.4	1104	649
M	136.7	53.4	49.5	688	321
A_b	35.4	21.8	15.4	247	77
A_o	52.6	23.6	18.8	281	103
A_p	55.5	25.9	19.9	304	105
B_b	23.6	10.3	6.4	112	30
B_o	31.4	12.8	8.3	139	39
B_p	28.9	12.6	7.9	136	37

[a] The "best filter" is the most sensitive for a 10 μJy flat spectrum source and the four galaxy models at $z = 3$, with the constraint that no filter extends bluer than 5.06 μm. All such filters cut on at 5.06 μm and extend to the cutoff wavelength listed.

[b] List of filter cutoff values (in μm), rather than S/N values.

The most sensitive Si:As filter is [5.06:7.4] but, as remarked above, the sensitivity is largely independent of the cutoff wavelength, dropping only 1% if we reduce the cutoff to 7 μm or raise it to 8.3 μm.

The optimum and preferred filters have a ~20% gain in sensitivity over the baseline specifications for a flat spectrum source. Figure 3 shows that the improvement holds for a fairly large range of spectral shapes, with the preferred A_p filter only losing out to the baseline A_b filter for spectra redder than $\alpha \gtrsim 3$ ($S_\nu \propto \nu^{-\alpha}$), due to the longer wavelength of the A_b filter.

3.2. High-Redshift Galaxies

Figure 4 plots the signal-to-noise ratio (S/N) achievable in 10 hr through Si:As filters for the four galaxy models at $z = 3$. Again, the contours are fairly vertical showing the

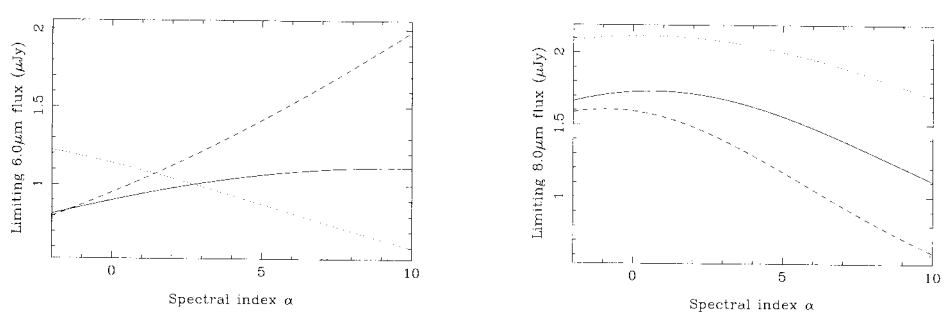

FIG. 3.—Limiting sensitivity (5 σ, 10 hr) for the preferred (*solid line*), optimum (*dashed line*), and baseline (*dotted line*) filters for power laws of the form $S_\nu \propto \nu^{-\alpha}$. *Left*: Filter *A*. *Right*: Filter *B*.

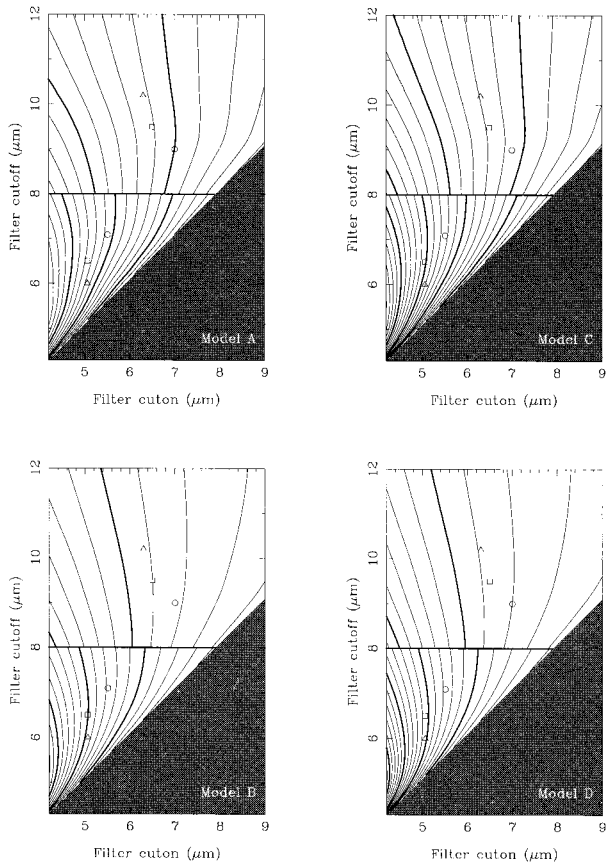

FIG. 4.—Contours of signal-to-noise ratio as a function of filter cut-on and cutoff in a 10 hr integration on the four galaxy models at $z = 3$. Symbols mark the filter specifications as in Fig. 2. Model A is contoured from 2 to 38 in steps of 2; model B from 2 to 34 in steps of 2; model C from 20 to 480 in steps of 20; and model D from 10 to 210 in steps of 10. Heavy contours are at multiples of 10, 10, 100, and 50, respectively.

cut-on wavelength is important and the S/N achievable is very insensitive to the cutoff. The best S/N at $z = 3$ for a Si:As filter is again with the bluest wavelength cut-on allowed (5.06 μm) and with a cutoff of 7.4, 6.1, 7.2, and 6.7 μm for models A, B, C, and D, respectively. Table 1 lists the signal-to-noise ratios achievable at $z = 3$ for the various Si:As filter choices.

The general conclusions thus far are that substantial improvements in sensitivity can be achieved over the baseline filter specifications by using a bluer *A* filter and a broader *B* filter. We show that this applies over a broad range of redshift in Figures 5 and 6, which plot the signal-to-noise ratio achievable in 10 hr for the three different filter pairs. For completeness, we show the S/N achievable through the two InSb filters as a function of redshift in Figure 7. The higher quantum efficiency of InSb and the lower background at short wavelengths produce an order of magnitude increase over what is achievable with the two Si:As arrays, but the need for the Si:As arrays will become clear in § 4.

3.3. The *SIRTF* Advantage

The advantage in using *SIRTF* to obtain an effectively mass-limited sample of high-redshift galaxies has already been stated. Here, we compare the sensitivities calculated above to the limits obtained, or obtainable, by other methods.

In Table 2, we first list the limits obtained, or obtainable, by deep exposures in the optical–infrared region. In Figure 8, we present the observed flux of a solar metallicity $z = 3$ L^* galaxy, which was formed in an instantaneous burst, through three different *Hubble Space Telescope* (*HST*) filters and our preferred IRAC filters, as a function of age. These fluxes correspond to model A where they intersect the right axis. From this, it is clear that optical selection methods, such as the "UV-dropout" technique, can only find galaxies which have undergone substantial star formation since $z = 4$ (i.e., similar to models C and D), as passive evolution since then will cause their UV flux to drop below a plausible detection threshold. Near-infrared observations fare rather better, although it should be noted that the Near Infrared Camera and Multi-Object Spectrometer (NICMOS) Hubble Deep Field catalog suffers significant incompleteness even at high signal-to-noise ratios (the 80% completeness limit is $m_{AB} \approx 26.7$ in both filters; Thompson et al. 1998). This F160W limit is sensitive enough to detect old, sub-L^* galaxies, and is comparable to the IRAC filters in this respect. However, the F110W filter, by virtue of its

TABLE 2

SENSITIVITIES (5 σ, 10 hr) OF INSTRUMENT/FILTER COMBINATIONS

Instrument/Filter	m_{AB}	S_ν (μJy)
HST WFPC2/F606W[a]	28.4	0.016
HST NICMOS/F110W[a]	27.2	0.047
HST NICMOS/F160W[a]	27.5	0.037
Subaru IRCS/K[b]	24.4	0.63
ISO CAM/LW-2[c]	20.4	24.7
SIRTF IRAC/L	25.6	0.21
SIRTF IRAC/M	25.0	0.36
SIRTF IRAC/A_p	24.0	0.90
SIRTF IRAC/B_p	23.3	1.73

[a] Scaled from observations of the Hubble Deep Field (Williams et al. 1996; Thompson et al. 1998).

[b] A description of Subaru Infrared Camera and Spectrograph (IRCS) can be found in Tokunaga et al. 1998.

[c] Scaled from Taniguchi et al.'s 1997 observations of the Lockman Hole.

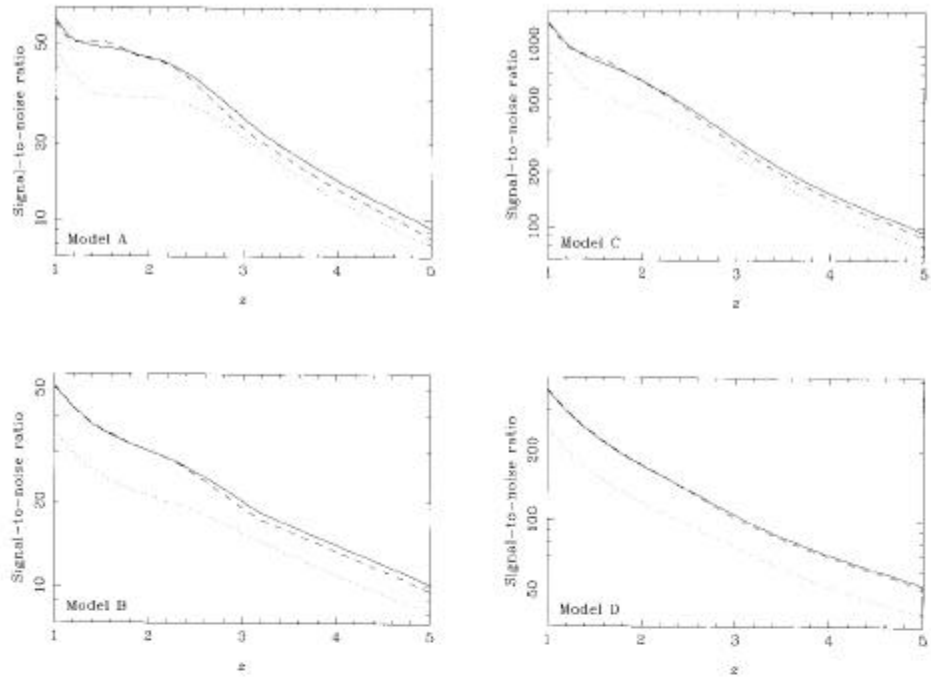

FIG. 5.—Signal-to-noise ratio (in 10 hr) for the three different A filters, as a function of redshift for the four galaxy models. *Solid line*: preferred (A_p); *dashed line*: optimum (A_o); *dotted line*: baseline (A_b).

sampling a region below the 4000 Å break, is far less sensitive, and obviously there is limited science which can be done from a single detection in one filter. In addition, the short rest-frame wavelengths which these filters probe are strongly affected by dust obscuration. IRAC will therefore be the first instrument capable of detecting distant, evolved L^* (and possibly even sub-L^*) galaxies, if they exist, at more than one wavelength. As a comparison, we note that the

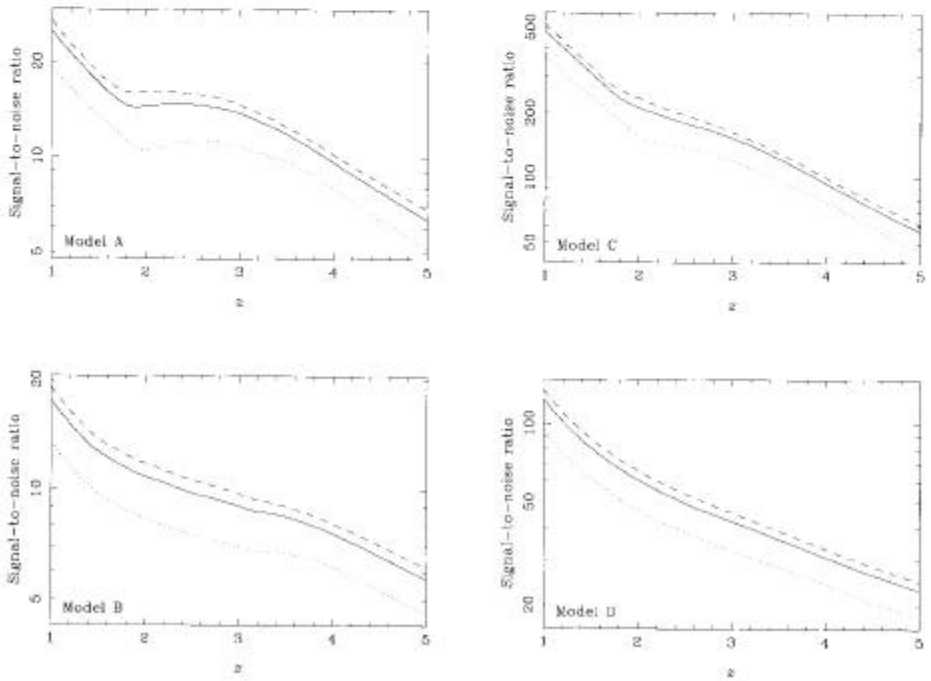

FIG. 6.—As Fig. 5, but for the three B filters

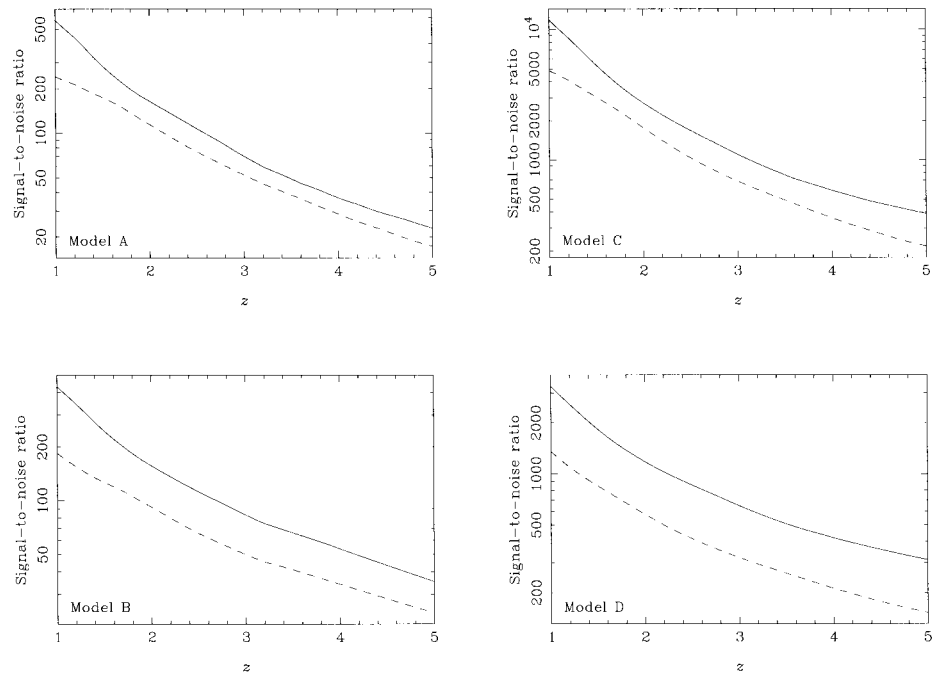

FIG. 7.—As Fig. 5, but for the InSb L (*solid line*) and M (*dashed line*) filters

deepest observations obtained by ISOCAM with the very wide LW-2 filter (5.0–8.5 μm) produced a much higher 5 σ limit of approximately 30 μJy in 6 hr of integration (13 hr of observation; Taniguchi et al. 1997).

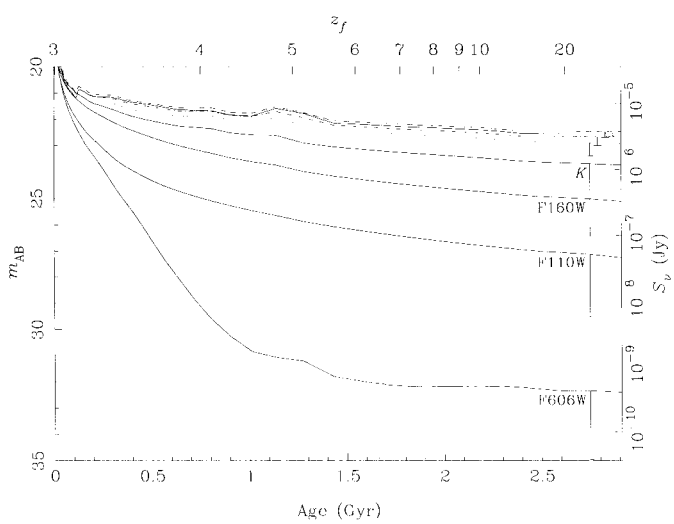

FIG. 8.—Observed flux for an L^* galaxy at $z = 3$ as a function of age (or formation redshift, z_f), through the filters *HST*/WFPC2 F606W, *HST*/NICMOS F110W, *HST*/NICMOS F160W, and ground-based K (all as labeled), and the four *SIRTF*/IRAC filters L (*dotted line*), M (*dot-dashed line*), A_p (*dashed line*), and B_p (*solid line*). The sensitivities of the filters are listed in Table 2 and the one-sided error bars indicate the amount of dimming caused by $A_V = 1$.

4. PHOTOMETRIC REDSHIFT DETERMINATION AT $z \sim 3$

In this section we present the analysis which defines the "optimum" filters and leads to our specifications for the "preferred" filters.

Two factors are important in deciding upon the best filters for photometric redshift determination. First, it is necessary to achieve a high signal-to-noise ratio in both filters, to allow the color to be determined accurately. This was discussed in the previous section. Second, this color must be a strong function of redshift, since the uncertainty in redshift, Δz, is related to the uncertainty in the color, $\Delta\Gamma$ (the color defined in the sense $\Gamma \equiv A - B$), by

$$\Delta z = (d\Gamma/dz)^{-1}\Delta\Gamma \, . \tag{1}$$

Figure 9 plots the $L-B$, $M-B$, and $A-B$ colors as a function of redshift for the four models. Magnitudes in each of the filters have been determined with respect to Vega (which we model as a 9400 K blackbody with a 2.2 μm flux of 657 Jy). It should be noted that at $z \lesssim 2$, the 3.3 μm PAH feature may affect the results since it will lie in the bandpass of filter B. It is apparent that the $L-M$ color is sensitive to redshift in the range $1 < z < 2$ (see the divergence between the $L-B$ and $M-B$ loci over this redshift range), due to the 1.6 μm bump moving through the filters. At higher redshifts the Si:As filters become increasingly important for measuring photometric redshifts. At $z > 2$, the increased separation

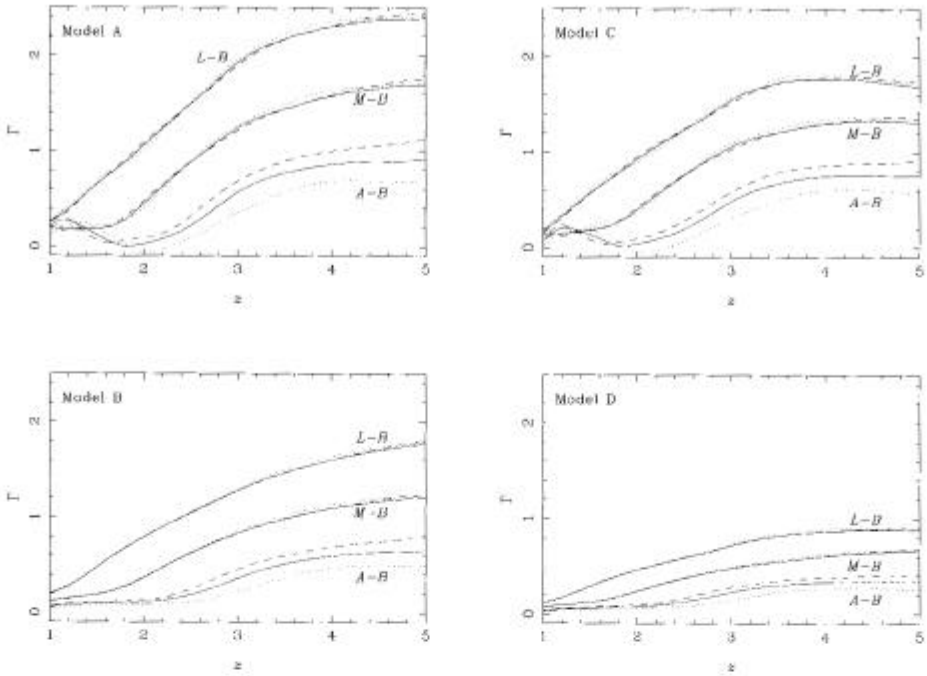

FIG. 9.—Colors as a function of redshift for the four galaxy models. *Solid lines*: preferred filters; *dashed lines*: optimum filters; *dotted lines*: baseline filters.

between the preferred and optimum A and B filters, compared to the baseline filters, causes them to produce larger color variations. Coupled with the increased sensitivity that these filters provide, it is clear that they will be able to produce more accurate photometric redshifts. We now quantify the level of this improvement.

The goal of photometric redshift determination is to minimize the uncertainty in the derived redshift, given by equation (1). We make a few approximations to ease the calculation of this function. First, we write $d\Gamma/dz \approx \Gamma(3.5) - \Gamma(2.5)$, and make use of the fact that for well-detected ($\gtrsim 5\ \sigma$) sources, the uncertainty in the measured magnitude $\Delta m \approx (\mathrm{S/N})^{-1}$, where S/N is the signal-to-noise ratio. We approximate the S/N (which varies slightly with redshift) as the geometric mean of the actual S/N at $z = 2.5$ and $z = 3.5$. In light of these rather crude approximations, we do not claim to be deriving accurate values of Δz, but instead present its reciprocal, which we call f (by plotting the reciprocal, we also avoid the infinities which arise when the color change between $z = 2.5$ and $z = 3.5$ is zero). For any two filters, X and Y, f is therefore defined as

$$f(X, Y) = [\Gamma(3.5) - \Gamma(2.5)] \Bigg/ \left[\frac{b_X}{c_X(3.5)c_X(2.5)} + \frac{b_Y}{c_Y(3.5)c_Y(2.5)}\right]^{1/2}, \quad (2)$$

where b_i is the total number of background counts and $c_i(z)$ the total number of object counts in filter i for a galaxy at redshift z. Large values of f are desired, and for photometric redshifts accurate to 10% at $z \sim 3$ ($\Delta z \lesssim 0.3$), $f \gtrsim 3$ is necessary.

We wish to find the specifications for the two Si:As filters that maximize $f(A, B)$. Unfortunately, since each filter needs two parameters to specify it, it is impossible to graphically present the results of this four-parameter optimization in a simple form. We therefore first consider the value of f for a single Si:As filter and the InSb M filter (the results are broadly similar if the L filter is used instead of M). Figure 10 is a contour plot of f for the M filter and an arbitrary Si:As filter whose specifications are given by the two axes. This figure favors a Si:As filter centered at $\sim 8\ \mu$m with $\sim 50\%$ bandwidth. Note that the contours are predominantly horizontal here, so that contrary to the S/N case, the long-wavelength cutoff is the most important parameter. A broad, long-wavelength filter is optimum for determining photometric redshifts at $z \sim 3$ even though the S/N it produces is not maximal.

We find the solution to the four-parameter optimization by performing a grid search throughout the available parameter space. We find that, irrespective of the particular galaxy model, the A filter always has the bluest cut-on allowed (5.06 μm). This is to be expected, since a blue A filter produces both high signal-to-noise ratio (Figs. 2 and 4) and a large color change over the redshift range of interest. The other parameters vary slightly between the four galaxy models, but an average solution is $A = [5.06:6.0]$ and $B = [6.3:10.2]$. This is the how we define the "optimum" filter choice referred to throughout this paper. The

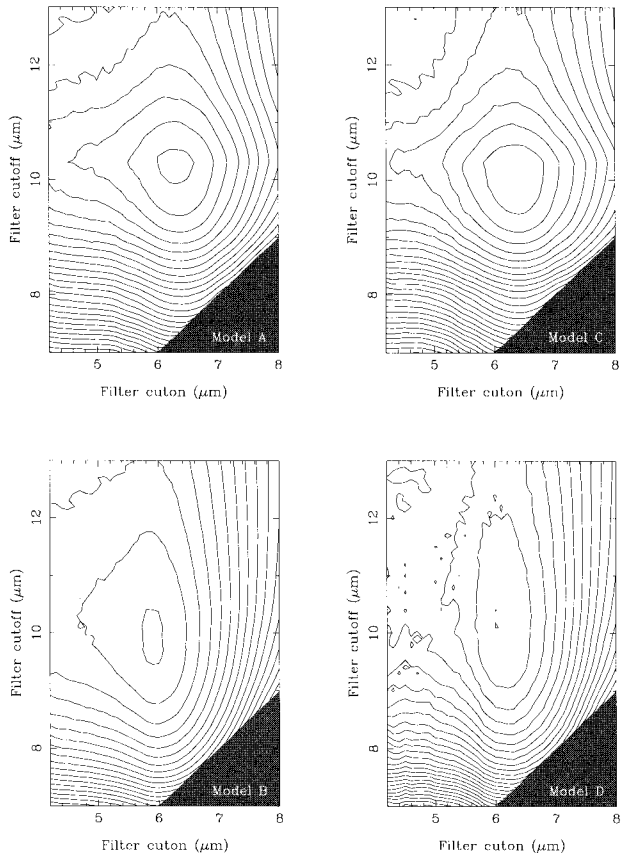

FIG. 10.—Contours of f (as defined in the text) for the InSb M filter and an arbitrary (ZnS coated) Si:As filter as defined by the axes of the plot, for each of the four galaxy models. Model A is contoured from -0.4 to 6.2 in steps of 0.2; model B from 0.0 to 3.1 in steps of 0.1; model C from -16 to 58 in steps of 2; and model D from -1.2 to 6.6 in steps of 0.2.

optimum B filter has a similar specification regardless of whether the color is formed using L, M, or A as the second filter.

Table 3 lists the values of f achieved for various pairs of filters. In terms of the value of this function, the optimum filters can produce an increase of as much as 60% in the accuracy of the photometric redshifts derived from the A and B filters, and a more modest (but still substantial) 20% improvement in accuracy when one of the InSb filters is used in conjunction with the B filter.

As an illustration of how photometric redshifts might be derived from IRAC data, in Figure 11 we present a $L-M$ versus A_p-B_p color-color plot for the four galaxy models in the redshift range $1 < z < 5$. It can be seen that the color in the two Si:As filters is generally able to provide an excellent measurement of the galaxy redshift for $z \gtrsim 2$. For $1 \lesssim z \lesssim 2$, the $L-M$ color provides most of the photometric redshift signal. Only Model D has a very limited range of colors which might hamper analysis, since we are observing the Rayleigh-Jeans tail of a recent starburst with only weak metal line blanketing; however, this is exactly the sort of UV-bright galaxy which would be detected in surveys for UV dropouts, and so this does not pose a problem.

TABLE 3

VALUES OF F FOR VARIOUS FILTER PAIRS

		f FOR MODEL			
FILTER 1	FILTER 2	A	B	C	D
Baseline Filters					
L	B_b	6.4	3.1	57	7.6
M	B_b	5.4	2.6	52	5.7
A_b	B_b	4.1	1.6	41	4.3
Optimum Filters					
L	B_o	7.6	3.7	66	9.1
M	B_o	6.2	3.1	59	6.6
A_o	B_o	6.0	2.8	63	6.7
Preferred Filters					
L	B_p	7.3	3.5	65	8.8
M	B_p	6.0	3.0	58	6.4
A_p	B_p	5.6	2.5	58	6.1
A_o	B_p	5.9	2.7	62	6.6

5. OTHER CONSIDERATIONS

Finally, we consider the impact of filter changes on two important aspects of distant galaxy detection which we have thus far ignored: confusion noise, which will ultimately limit *SIRTF*'s sensitivity, and dust, which is not included in the Bruzual & Charlot spectral synthesis models.

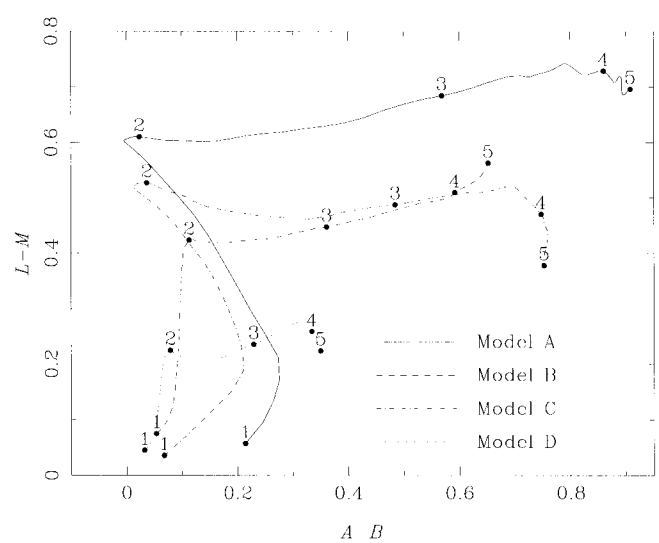

FIG. 11.—Loci of the four galaxy models discussed in the text in the $L-M$ vs. A_p-B_p color-color diagram. The locations of the models at $z = 1, 2, 3, 4, 5$ are indicated.

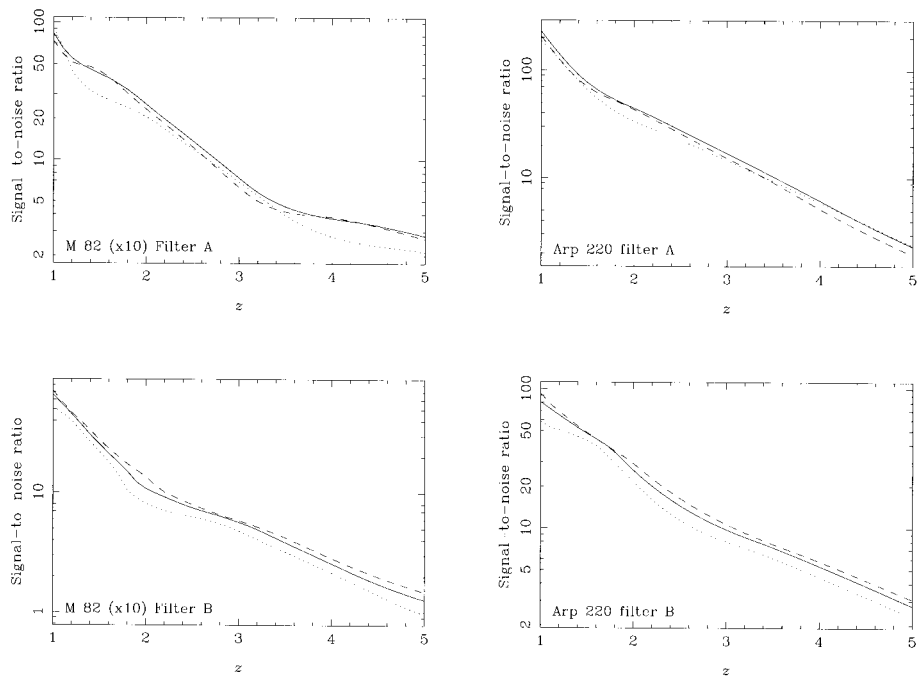

FIG. 12.—Signal-to-noise ratio (in 10 hr) for redshifted versions of the starburst galaxies M82 and Arp 220. M82 has been scaled up by a factor of 10 in luminosity. *Solid lines*: preferred filters; *dashed lines*: optimum filters; *dotted lines*: baseline filters.

5.1. Confusion Noise

Confusion noise is expected to limit IRAC sensitivity to ~ 0.5 μJy (1 σ; Franceschini et al. 1991), although this number is quite uncertain and model dependent. The confusion noise also depends on the source density and the beam size, both of which are wavelength dependent. Of particular concern is how much the density of confusing sources will increase over the baseline filter with a new B filter, due to a longer cutoff wavelength. The longer cutoff may significantly increase confusion because it includes the strong, broad 7.7 μm PAH feature (e.g., Uchida, Sellgren & Werner 1998) out to $z \sim 0.5$, a large enough distance that substantial volume is sampled and evolving dwarf galaxies may dominate the counts.

Franceschini et al. (1991) estimate the density of sources at 6.7 μm, and their prediction of ~ 1.2 arcmin^{-2} above a flux level of 30 μJy is consistent with Taniguchi et al.'s (1997) detection of 15 such sources in a $3' \times 3'$ field. At microjansky flux levels, most sources will be at $z \gtrsim 1$, so we use the spectrum $S_\nu \propto \nu^{-0.3}$ displayed at rest wavelengths ~ 3 μm to convert a limiting 8 μm flux to a 6.7 μm flux. Our best estimate of the total number of sources above 0.5 μJy at 8 μm is therefore ~ 100 arcmin^{-2}, which is ~ 0.8 sources per 20 pixel detection area. We estimate the number of PAH-emitting galaxies from the cirrus/photodissociation region spectrum and local 15 μm luminosity function of Xu et al. (1998). Even with very strong $[(1 + z)^4]$ evolution, the number of sources with $z < 0.5$ above 0.5 μJy is no more than 10 arcmin^{-2}, a small fraction of the total confusing source density.

We also note that the longer cutoff wavelength of the new B_p filter does not produce a significant increase in the diffraction-limited beam size for a range of spectral slopes, compared to the B_b filter (N. Gautier 1998, private communication). The confusion noise will therefore not be increased and the overall performance of the filter will not be affected.

Finally, we note that the confusion noise limit of 0.5 μJy would limit the ultimate values obtainable for $f(A_p, B_p)$ (as defined in eq. [2]) to 3.2, 1.5, 34, and 3.7 for Models A, B, C, and D, respectively. In the confusion-limited case, where the photometric accuracy is largely independent of the filter choice, it can be argued that one should attempt to maximize the product of the photometric redshift accuracy and the sky area which can be surveyed in a given time. This produces slightly different specifications for the optimum B filter ([6.0:10.1] instead of [6.3:10.2]) although the arguments of § 6 lead to the same final choice of "preferred" filters.

5.2. Dusty Galaxies

Nearby starburst galaxies, e.g. M82 and Arp 220, are very dusty and have red near-infrared spectra, as well as strong PAH emission features. Our choice of a bluer A filter might therefore impair our ability to detect similar objects at high

redshift, which would be cosmologically very interesting. Figure 3 shows that for spectra redder than $\alpha \gtrsim 3$, the A_b filter is more sensitive than A_p. In Figure 12 we show the sensitivities of the three different filter pairs to these two starburst galaxies as a function of redshift (the spectrum of M82 has been scaled up by a factor of 10 in luminosity in this figure). The spectral energy distributions required to make these figures were produced with photometric data culled from a variety of sources, and aperture matching using curve-of-growth analysis was required. This is likely to produce errors where the spectral region sampled by a given filter includes the transition between different data sets (e.g., optical and near-infrared), and the signal-to-noise ratios (both absolute and relative) should probably not be trusted to more than $\sim 10\%$. Given these caveats, there is little to choose between the different A filters, but the sensitivity improvement offered by the B_p filter is unambiguous.

6. CONCLUSIONS: THE "PREFERRED" FILTERS

Although the broad B_o filter is supported by sensitivity calculations and does not suffer significantly from increased confusion noise, a somewhat narrower filter makes sense for other reasons. The almost 50% bandwidth of the B_o filter will make photometry difficult and may compromise other uses of this filter. In particular, the strong silicate absorption feature at 9.7 μm falls in the B_o bandpass. We therefore recommend a shorter cutoff wavelength, and propose $B = [6.5:9.5]$ (a 37% bandpass) as our "preferred" B filter, B_p.

Conversely, the optimum $A_p = [5.06:6.0]$ choice is only a 17% bandwidth, and does not produce optimum S/N (see Table 1). It does however avoid the PAH feature at 6.2 μm, offering the possibility of using filters A and B as a PAH diagnostic. However the M filter also acts as a good continuum filter for this problem, with better S/N and the advantage that it shares the same field as the B filter. Hence we recommend a broader A filter filling the wavelength regime between M and B. Our preferred A filter, A_p, is then $[5.06:6.5]$, with a 25% bandpass.

These preferred filters reduce the value of f by about 10%, compared to the optimum filters, but we feel that this is outweighed by the gain in general scientific usefulness. In any case, they still offer a significant improvement over the baseline 6.3 and 8.0 filters. These specifications have now been adopted for the IRAC instrument.

The authors wish to thank Roc Cutri, Nick Gautier, Craig McCreight, and Harvey Moseley for their help. This work was performed at the Jet Propulsion Laboratory, California Institute of Technology, under a contract with the National Aeronautics and Space Administration.

REFERENCES

Barger, A. J., Cowie, L. L., Sanders, D. B., Fulton, E., Taniguchi, Y., Sato, Y., Kawara, K., & Okuda, H. 1998, Nature, 394, 248
Bruzual A., G., & Charlot, S. 1993, ApJ, 405, 538
———. 1999, in preparation
Charlot, S., Worthey, G., & Bressan, A. 1996, ApJ, 457, 625
Fanson, J., Fazio, G., Houck, J., Kelly, T., Rieke, G., Tenerelli, D., & Whitten, M. 1998, Proc. SPIE, 3356, 478
Fazio, G., et al. 1998, Proc. SPIE, 3354, 1024
Franceschini, A., Toffolatti, L., Mazzei, P., Danese, L., & De Zotti, G. 1991, A&AS, 89, 28
Gardner, J. P., Sharples, R. M., Frenk, C. S., & Carrasco, B. E. 1997, ApJ, 490, L99
Gavazzi, G., Pierini, D., & Boselli, A. 1996, A&A, 312, 397
Hauser, M. G. 1996, in AIP Conf. Proc. 348, Unveiling the Cosmic Infrared Background, ed. E. Dwek (New York: AIP), 11
Hauser, M. G., et al. 1998, ApJ, 508, 25
Hogg, D. W., et al. 1998, AJ, 115, 1418
Hughes, D. H. et al. 1998, Nature, 394, 241
John, T. L. 1988, A&A, 193, 189
Kawara, K., et al. 1998, A&A, 336, L9
Madau, P., Ferguson, H. C., Dickinson, M. E., Giavalisco, M., Steidel, C. C., & Fruchter, A. 1996, MNRAS, 283, 1388
Puget, J. L., et al. 1999, A&A, in press
Salpeter, E. E. 1955, ApJ, 121, 161
Schmidt, M., Schneider, D. P., & Gunn, J. E. 1995, AJ, 110, 68
Steidel, C. C., & Hamilton, D. 1992, AJ, 104, 941
———. 1993, AJ, 105, 2017
Steidel, C. C., Adelberger, K. L., Giavalisco, M., Dickinson, M., & Pettini, M. 1999, ApJ, in press
Steidel, C. C., Giavalisco, M., Pettini, M., Dickinson, M., & Adelberger, K. L. 1996, ApJ, 462, L17
Taniguchi, Y., et al. 1997, A&A, 328, L9
Thompson, R. I., Storrie-Lombardi, L. J., Weymann, R. J., Rieke, M. J., Schneider, G., Stobie, E., & Lytle, D. 1998, AJ, 117, 17
Tokunaga, A. T., et al. 1998, Proc. SPIE, 3354, 512
Uchida, K. I., Sellgren, K., & Werner, M. 1998, ApJ, 493, L109
Williams, R. E., et al. 1996, AJ, 112, 1335
Wright, E. L., Eisenhardt, P., & Fazio, G. 1994, AAS, 26, 893
Xu, C., Hacking, P. B., Fang, F., Shupe, D. L., Lonsdale, C. J., Lu, N. Y., & Helou, G. 1998, ApJ, 508, 576